MIT Libraries | DSpace@MIT

MIT Open Access Articles

Power handling of silicon microring modulators

Massachusetts Institute of Technology

Power handling of silicon microring modulators

Marc de Cea,* Amir H. Atabaki, and Rajeev J. Ram

Research Laboratory of Electronics, Massachusetts Institute of Technology, Cambridge, Massachusetts 02139, USA

*mdecea@mit.edu

Abstract: Silicon photonic wavelength division multiplexing (WDM) transceivers promise to achieve multi-Tbps data rates for next-generation short-reach optical interconnects. In these systems, microring resonators are important because of their low power consumption and small footprint, two critical factors for large-scale WDM systems. However, their resonant nature and silicon's strong optical nonlinearity give rise to nonlinear effects that can deteriorate the system's performance with optical powers on the order of milliwatts, which can be reached on the transmitter side where a laser is directly coupled into resonant modulators. Here, a theoretical time-domain nonlinear model for the dynamics of optical power in silicon resonant modulators is derived, accounting for two-photon absorption, free-carrier absorption and thermal and dispersion effects. This model is used to study the effects of high input optical powers over modulation quality, and experimental data in good agreement with the model is presented. Two major consequences are identified: the importance of a correct initialization of the resonance wavelength with respect to the laser due to the system's bistability; and the existence of an optimal input optical power beyond which the modulation quality degrades.

1. Introduction

Silicon photonic optical interconnects [1] promise to meet the growing demands in communication bandwidth thanks to their scalability, high bandwidth density and low loss. Key to achieving such high data rates is the ability to carry and manipulate multiple data streams carried by closely-spaced wavelengths in a single waveguide or fiber, in what is known as dense wavelength division multiplexing (DWDM) [2]. The microring resonator arises as a promising element in these systems due to its small footprint, low power consumption and narrow wavelength selectivity [3], allowing for independent manipulation of each wavelength by cascading microrings on an optical bus [4]. High-speed modulation can be obtained with ring resonators by shifting its resonance wavelength through a change in its carrier density, and therefore refractive index [5], by applying an external voltage to a pn junction embedded in the device [6,7].

Nevertheless, ring-based DWDM systems are challenging due to their narrow-band nature that makes them highly sensitive to fabrication variations and environmental fluctuations (e.g., substrate temperature). In addition, the strong light confinement and electric field enhancement exhibited in these structures due to their high quality factors and small sizes gives rise to high optical power densities, which combined with high third-order nonlinearity in silicon [8], generate nonlinear effects that can cause unwanted behavior even for moderate input optical powers on the order of mW. Effects such as thermal [9] and carrier [10] induced optical bistabilities, as well as self-pulsation due to the competition between these processes [11], have been reported in silicon microring or microdisk resonators.

As the loss of specific components in a communications link (such as grating couplers, modulators or detectors) become more difficult to improve, the push for longer link distances and improved link budgets will require an increase in input optical powers, exacerbating the issues associated to handling high powers in general, and particularly in resonant modulators. As a consequence, understanding the behavior of resonant modulators under high optical powers

becomes key for the design and operation of practical DWDM systems for the data center and telecommunication spaces.

Time domain models have been developed to study nonlinear effects in silicon resonators. In [11], Johnson et al. presented a model accounting for the effects of two photon absorption (TPA), free carrier absorption (FCA) and self-heating. A similar model focusing on carrier effects was also presented in [12]. These models are developed for passive structures, in which no active external modulation of the device resonance is possible. Here, a time domain model for externally modulated silicon resonators is implemented which accounts for the main nonlinearities that affect modulation performance – free carrier dispersion, FCA, TPA and thermal effects – and is used to study power handling limits in silicon microring modulators (Fig. 1(a)). We apply this model to our CMOS photonic microring modulators and demonstrate that modeling results are in good agreement with experiments, confirming the validity of the derived model.
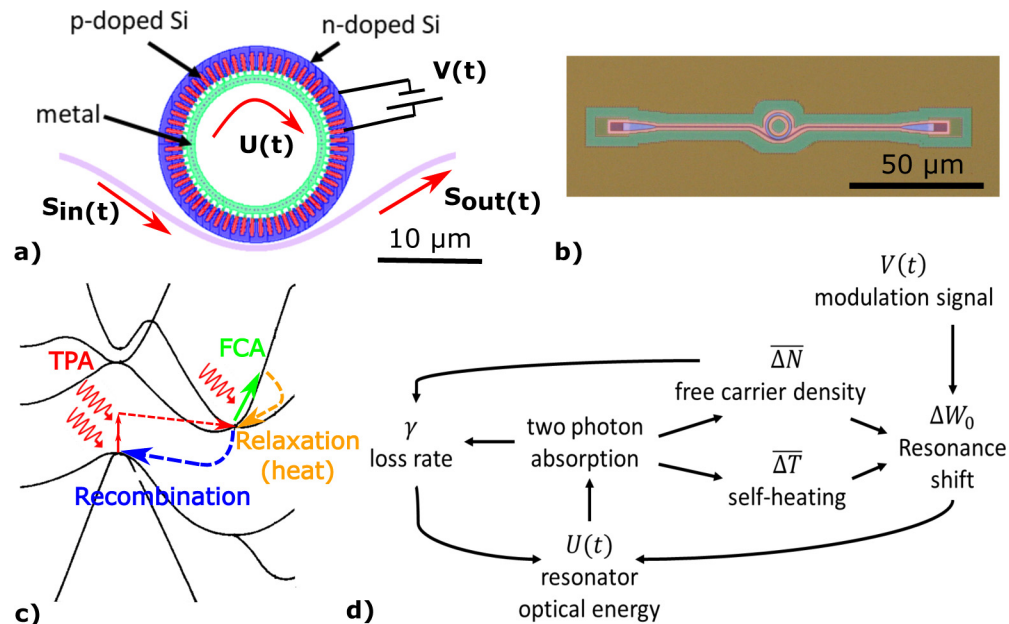

Fig. 1. (a) Top view of the modeled resonant modulator. $S_{in}(t)$ and $S_{out}(t)$ represent the input and output optical E-fields, and $U(t)$ is the energy stored in the microring. $V(t)$ is the modulator's driving signal. (b) Optical micrograph of the ring resonator used in the experiments. (c) Diagram of the physical phenomena occurring in a silicon optical device in the presence of two photon absorption (TPA). (d) Diagram of nonlinear effects in a silicon ring modulator and their inter-dependence. The modulation signal ($V(t)$) changes the resonance frequency (ΔW_0) of the device, affecting the total stored energy in the resonator and setting the strength of TPA. TPA, in turn, modifies the resonance through two effects: free-carrier dispersion and self-heating. These two phenomena compete in opposite directions: free carrier dispersion shifts the resonance to shorter wavelengths, while heating pushes it to longer wavelengths.

2. Theoretical model

In [11], Johnson et al. presented a time domain model to describe nonlinear effects in passive high quality factor (Q) silicon resonant structures. There, TPA, FCA and self-heating were accounted for: TPA results in photon loss and the generation of free carriers (which in turn induces more optical loss through FCA), and free-carrier dispersion that shifts the resonance to

shorter wavelengths. All of the absorption mechanisms cause a heating of the device, inducing thermo-optic dispersion that shifts the resonance to longer wavelengths. The combination of these effects (Fig. 1(c)) results in behaviors such as bistability and self-pulsation in the resonator. In this work, Johnson's model is extended to include active modulation of the resonator with an applied external voltage. Figure 1(d) depicts the physical processes considered in this work (TPA, FCA, thermal dispersion, carrier dispersion and external modulation) and the intricate coupling between them. This model allows us to analyze the behavior of free-carrier-plasma-dispersion microring modulators in the presence of nonlinear effects.

A detailed derivation of the nonlinear model based on coupled-mode theory can be found in [11]. Here, we have included three modifications to the model to extend it to actively modulated devices. First, the splitting between clockwise and counterclockwise modes of the ring is not considered, since this effect is only observable in high quality factor (Q >100, 000) resonators that are not attractive for fast modulation due to their limited bandwidth [18] (optimal Q for high-speed modulation are in the 10,000-20,000 range). Second, the definitions of effective mode volumes for TPA (V_{TPA}) and FCA (V_{FCA}), and of the field confinement factor (Γ_{ring}) have been modified by normalizing the electric field to the Poynting vector rather than the E-field energy for better accuracy in high-index-contrast silicon photonic structures [19]. Third, the effect of external modulation voltage on the resonance frequency of the microring ($\Delta W_{0_{mod}}$) is included as an additive term next to the thermal and plasma dispersion terms:

$$\frac{\Delta W_0(t)}{W_0} = -\frac{1}{n_{Si}}\left(\frac{dn_{Si}}{dT}\overline{\Delta T(t)} + \left(\frac{dn_{Si}}{dN_p} + \frac{dn_{Si}}{dN_n}\right)\overline{N(t)}\right) + \frac{\Delta W_{0_{mod}}(t)}{W_0} \tag{1}$$

We assume the resonance frequency changes linearly with the pn junction voltage through dW_0/dV_{pn}, a valid assumption for most high-speed modulators due to high doping concentrations that lead to very small changes in the depletion width compared to the optical mode size:

$$\Delta W_{0_{mod}}(t) = \frac{dW_0}{dV_{pn}}V_{pn}(t) \tag{2}$$

The voltage across the pn junction (V_{pn}) whose depletion region is modulated through $V(t)$ is modeled as a first order system with time constant τ:

$$\frac{dV_{pn}(t)}{dt} = \frac{-V_{pn}(t)}{\tau} + \frac{V(t)}{\tau} \tag{3}$$

Due to the dependence of the depletion capacitance ($C(t)$) and series resistance ($R(t)$) of the device on the applied voltage, the time constant τ is time dependent. Nevertheless, this dependence is very small due to the high doping concentrations used in these devices and is considered negligible in this work.

A variable order Adams-Bashforth-Moulton predictor-corrector method [20] has been used to solve the coupled nonlinear model. We solve for the time evolution of the optical signal at the output of the modulator and that of the resonator variables (resonance wavelength, stored energy, temperature, etc.) as a binary (i.e., on-off keying) electrical voltage signal is applied to the modulator, allowing for the visualization of the time-domain behavior of the modulator and giving insight into its operation in the nonlinear regime (see Figs. 4 and 5).

3. Optical modulator under study

In this work, we will study a depletion-type pn-junction silicon ring modulator designed for a wavelength of 1550 nm. The ring has an outer radius of 10 μm, is 1.7 μm wide and roughly 100 nm thick [21] (Figs. 1(a) and 1(b)). This device was fabricated in a commercial microelectronic foundry (45nm SOI CMOS process node) using the 'zero change' CMOS approach [22]. High speed operation up to 25 Gbps of this device has been demonstrated in [16].

Table 1. Model parameters corresponding to the silicon microring modulator studied in this work. FEM = Finite Elements Method [13,14,15].

Parameter	Value	Source	Parameter	Value	Source
β_{Si}	8.4×10^{-12} $m \cdot W^{-1}$	[8]	n_{Si}	3.485	[13]
dn_{Si}/dT	1.86×10^{-4} K^{-1}	[14]	dn_{Si}/dN_n	-8.8×10^{-22} cm^3	[5]
dn_{Si}/dN_p	-8.5×10^{-18} cm^3	[5]	α_p	6×10^{-22} m^2	[5]
α_n	8.5×10^{-22} m^2	[5]	Γ_{TPA}	0.90967	FEM
Γ_{FCA}	0.9621118	FEM	Γ_{ring}	0.6515	FEM
V_{FCA}	8.67×10^{-18} m^3	FEM	V_{TPA}	10.63×10^{-18} m^3	FEM
γ_0	30 GHz	DC transmission	γ_{rad}	11 GHz	DC transmission for different input powers [15]
κ	1.73×10^5 $\sqrt{Hz}$	DC transmission	n_g	2.73	Free spectral range
dW_0/dV_{pn}	1.57×10^{10} $rad/(s \cdot V)$	DC transmission for different voltages	γ_{th}	2.4 MHz	DC transmission for different input powers
τ	10 ps	Bandwidth measurements [16]	γ_{lin}	19 GHz	DC transmission for different input powers [15]
γ_{fc}	10 GHz	[17]	λ_0	1545.2 nm	DC transmission
$V(t)$ signal	$2^7 - 1$ PRBS square	Arbitrary	$V(t)$ data rate	0.5 $Gbps$	Arbitrary
$V(t)$ bias voltage	-2.5 V	Arbitrary	$V(t)$ amplitude	4 V_{pp}	Arbitrary

In the time-domain nonlinear model, different physical parameters capture linear and nonlinear effects in the resonator. These parameters are listed in Table 1 along with a brief description for their derivation for the device under study. An important parameter in our model is the free-carrier lifetime, which is estimated to be on the order of 0.1 ns in our device [17]. This magnitude is consistent with the estimated lifetime from operation of the device in the forward bias regime, and lifetime variations on the order of 0.5-5x do not cause significant differences in the qualitative behavior of the model. The thermal time constant γ_{th} has been derived using the estimates for the thermal impedance (through self-heating resonance shift measurements) and heat capacitance of the device.

4. Results

The model described in the previous sections allows us to obtain the time domain optical waveform at the output of the modulator device $s_{out}(t)$, allowing direct comparison between modulation results under different operational conditions. Here, the optical modulation amplitude (OMA) will be used as a measure of the quality of the modulation, as it can be directly related to the bit error rate (BER) in a communication link [24]. The OMA is defined as the difference between the mean value of the '1' (μ_1) and '0' (μ_0) bits, and can be rewritten as $\mu_1 - \mu_0 = \frac{P_{in}}{IL}\left(1 - \frac{1}{ER}\right)$, where P_{in} is the input optical power, and *ER* and *IL* are the extinction ratio and insertion loss of the modulator, respectively.

4.1. Device initialization

The presence of bistabilities under high optical powers makes it important to bring the resonator into a stable point before starting the modulation. Figure 2(a) shows the bistability curve of the device for a 0.45 mW optical power launched in the input waveguide, simulated using [23]. The red shift of the resonance (λ_0) in states A and B is observed due to the thermal effect.

By tracking the resonance along the A+B branch through sweeping the laser (λ) from shorter wavelengths, the laser can be placed on any arbitrary point on the blue side of the Lorentzian curve of the resonator. This is shown by the blue curve in Fig. 2(b), which shows the transmission value simulated with our time domain model as wavelength is swept from the blue side of the resonance toward longer wavelengths. The consequence of this initialization approach is that it allows us to achieve an arbitrary small value for the transmitted zero bit (μ_0) and therefore high ER and high OMA modulation.
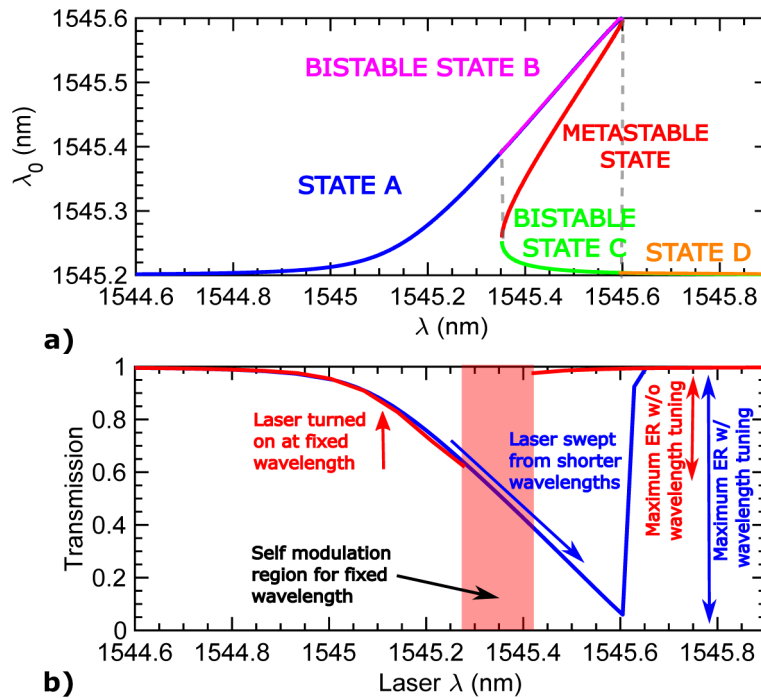
Fig. 2. Device initialization. (a) Bistability curve of the microring extracted using the model in [23] for a 0.45 mW input power. λ_0 is the resonance wavelength of the ring and λ is the laser wavelength. (b) Transmission as a function of wavelength for a 0.45 mW input optical power obtained with the model presented in this work. Red curve corresponds to the laser being abruptly turned on at a fixed wavelength, and the blue curve corresponds to the laser being swept from the blue side of the resonance and stopped at the target wavelength. The ER achievable when the laser is swept is considerably higher.

However, if instead the laser is not swept but is abruptly turned on at a given wavelength, the ability to track the resonance is lost, causing a transition from branch A in the blue side of the resonance to branch C in the red side. This is shown by the red curve in Fig. 2(b), which was again obtained by solving the nonlinear model presented above. It is seen that as opposed to the swept initialization case (blue curve), when the laser is directly turned on at the target wavelength the transmission values cannot approach zero, resulting in a low OMA modulation and therefore high BER. Furthermore, when the laser is turned on abruptly self-modulation due to competing heating (moving the resonance to longer wavelengths) and free-carrier (moving the resonance to shorter wavelengths) dispersion can occur (shaded band in Fig. 2(b)), preventing successful data modulation.

Note that the same initialization (tracking down the A+B branch) is used for most nonlinear experiments with high-Q resonators, as the goal in those experiments is to achieve maximum power drop in the resonator for maximizing the nonlinearity [25], which overlaps with our goal to achieve low '0' bit values (strong power drop) for modulation.

4.2. *Power handling: optimal operational point*

Using our time-domain nonlinear solver, we explored power handing capabilities of the microring modulator as the device is driven by a pseudo-random bit sequence with the characteristics specified in Table 1. Different input optical powers and optical carrier (laser) wavelengths (swept from the blue side of the resonance as mentioned in the previous section) were considered, and

the modulation performance metrics (ER, IL, OMA) were extracted by analyzing the obtained time-domain transmission waveforms.

To confirm the validity of the model, the same study was performed experimentally on the device described in Section 3 under the same operational conditions as the simulation. The modulator's output optical signal for different input optical powers and laser wavelengths was recorded using a photodetector connected to a high speed oscilloscope and analyzed to extract modulation performance metrics. To reach high input optical powers an Erbium Doped Fiber Amplifier (EDFA) was used to amplify the light coming out of a tunable laser, and a second EDFA was used at the output of the modulator device to increase the strength of the signal going into the photodetector. A narrowband filter was used to reduce the Amplified Spontaneous Emission (ASE) noise at the output of the second amplifer. Nevertheless, to avoid the insertion loss hit in the input optical power ($\approx 6\,dB$), no ASE filter was used after the first EDFA at the input of the device.

Figures 3(a) and 3(b) show the evolution of ER, IL and OMA with wavelength for a fixed input optical power of 0.45 mW and a 4 V_{pp} driving voltage derived with the model (Fig. 3(a)) and obtained experimentally (Fig. 3(b)). OMA results are normalized to its maximum to allow for a direct comparison between experimental OMA (measured in mV at the output of the photoreceiver) and simulated OMA (given in mW at the output of the microring).
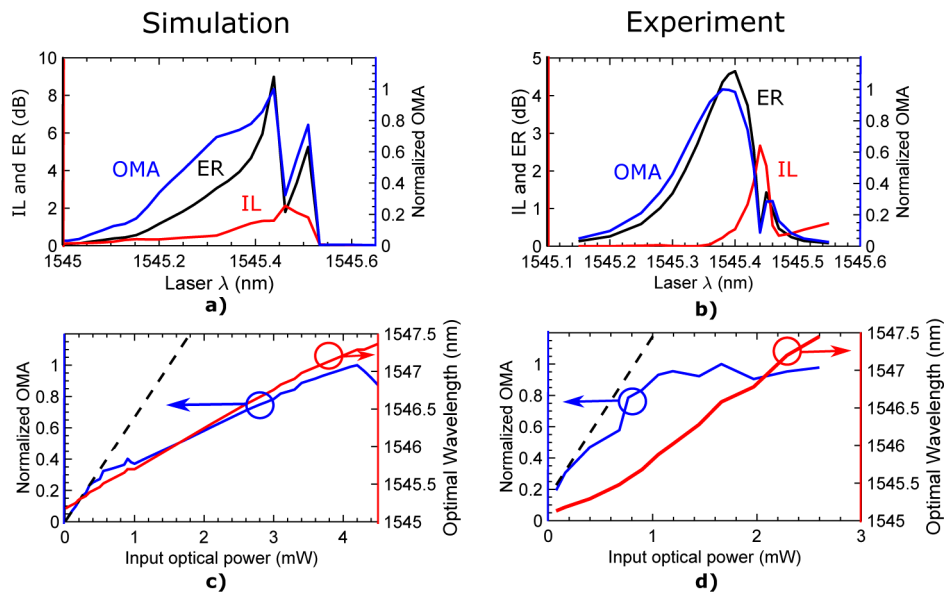

Fig. 3. Device optimum operational point. Theoretical (a) and experimental (b) evolution of the ER (black), IL (red) and normalized OMA (blue) as a function of laser wavelength for a 0.45 mW input power. Theoretical (c) and experimental (d) maximum attainable OMA (blue, left axis) and wavelength at which this value is reached (red, right axis) as a function of input power. The dashed line shows the expected evolution of OMA if no nonlinearities were present. Reported experimental powers are at the center laser wavelength and do not account for the extra input power due to unfiltered ASE optical power coming from the EDFA. The data rate used is 0.5 Gbps.

The results given by the model are in good agreement with the experimental curves. The existence of two distinct peaks (corresponding to modulation in the blue (peak at lower wavelengths) and red (peak at higher wavelengths) sides of the ring resonance) for OMA and ER is correctly modeled, as well as the fact that the maximum IL occurs between these two peaks (due

to modulation happening right at the resonance dip). The model also correctly captures the fact that better OMA is obtained when modulation is performed at the blue side of the resonance, and that the maximum OMA is obtained when the ER is maximum. Due to the theoretical model not accounting for noise, experimental ER (IL) values are lower (higher) than theoretical values. For the same reason, experimental curves show a smoother dependence with wavelength.

Both experiment and theory show that there is a well-defined wavelength where the best performance is achieved for a specific input optical power. As expected, the IL is near zero when the laser is far from the 'hot' resonance of the device (the resonance under nonlinear effects), and increases and reaches a peak as it approaches the transmission dip (where the modulation swing is not enough to move the device out of the resonance line-shape). The ER increases as the laser approaches the resonance dip from the blue side, and reaches a maximum when the system is able to reach the critical coupling condition and close to zero transmission for bit '0'. As the laser moves slightly to longer wavelengths, ER drops dramatically as the modulation now happens between the two sides of the resonance lineshape, resulting in a return-to-zero (RZ) like pattern with a high '0' output power. ER increases and reaches a second peak as modulation moves completely to the red side of the resonance, but the value of ER is low due to the resonance returning quickly to its cold state (state D in Fig. 2(a)).

Figures 3(c) and 3(d) show the highest achieved OMA (blue curve; normalized to its maximum to allow for comparison of experimental and theoretical results) along with the wavelength (red curve) at which it is achieved derived with the model (Fig. 3(c)) and obtained experimentally (Fig. 3(d)). Again, good qualitative agreement between experimental and theoretical results is achieved: (1) the experimental optimal operational wavelengths are very closely reproduced by our model, and (2) the saturation and eventual decrease in the maximum attainable OMA as input optical power increases, which is predicted by the theoretical model, is also observed experimentally, although not as clearly.

While simulated data shows a peak in OMA followed by a saturation (see Fig. 5(a)), experimental data only shows the saturation of OMA. Notice how, in simulation, the difference between the peak OMA and its saturated value is roughly 20%, or 1dB. We believe that we could have missed this relatively small peak due to our coarse choice of wavelengths in the experiment. Nevertheless, both the theory and experiment point to presence of an optimum input optical power: if the maximum attainable OMA has plateaued, there is no need to increase the power as this will only increase power consumption but won't improve modulation quality.

The existence of nonlinear effects results in an optimal input optical power for modulation quality: an increase in the power beyond this limit will deteriorate the performance due to the enhancement of nonlinear effects. Note that, if nonlinearities were not present in the system, OMA would linearly increase with input power (dashed black curves in Fig. 3(c) and 3(d)) as ER and IL would be independent of the optical power (resulting in OMA being only dependent on P_{in}). In the presence of nonlinearities, there is a power above which the negative effects of increased thermal and carrier dispersion (which cause a fluctuation in the output power values for bits '1' and '0', see Fig. 4) overcome the gain of using a high input power that would otherwise result in a higher '1' output power and an improvement in OMA.

As can be observed, the theoretical optimal input power (≈ 4.2 mW) is around 2.5x higher than the experimentally measured optimum (≈ 1.65 mW). This difference is due to the fact that the experimental powers measured and reported correspond to the power at the center wavelength of the laser, but the effective power entering the cavity is higher due to the presence of unfiltered ASE optical power. By studying the shift in resonance wavelength as a function of input optical power with and without an input EDFA, we observed that the total effective power driving nonlinearities was approximately 2-3 dB higher than the center wavelength input power. Additionally, uncertainties in the input grating coupler loss (which translate into uncertainties in
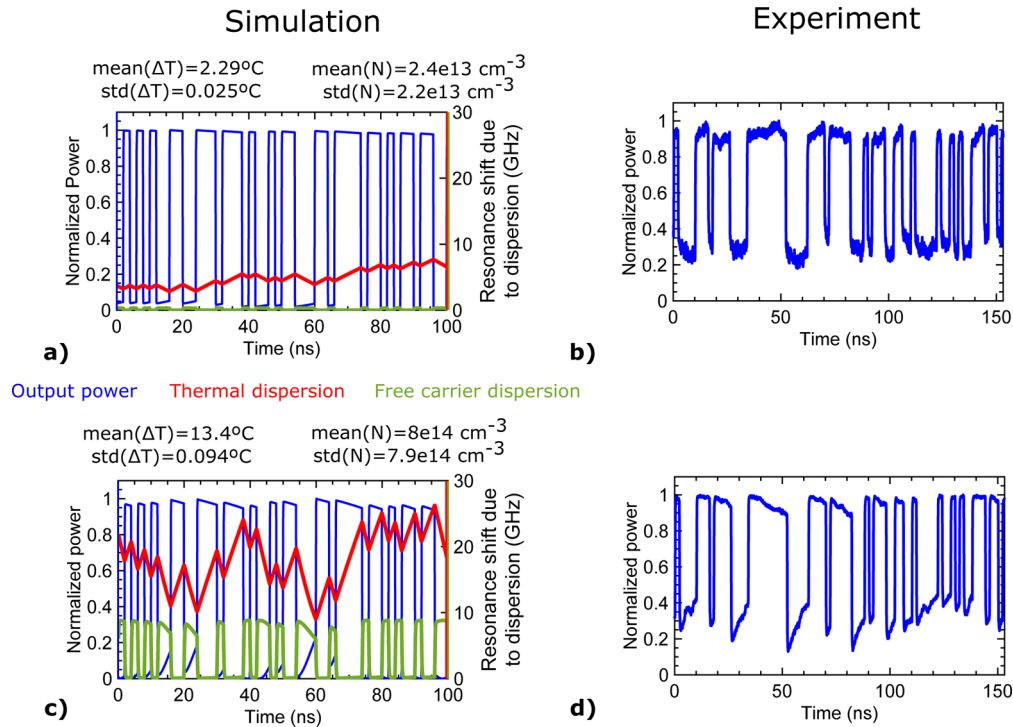
Fig. 4. Effects of nonlinearities in time domain. Simulated normalized output optical power as a function of time (blue, left axis) and resonance frequency shift due to temperature (red, right axis) and carrier density (green, right axis) fluctuations for 0.3 mW input optical power (a) and for 2 mW input optical power (c). Resonance shifts are referenced to the minimum shift for the operational condition being considered, so that the shown curves are $\Delta W_X(t) - min\{\Delta W_X(t)\}$, where X refers to either temperature or carrier dispersion. Experimental normalized output optical power as a function of time for 0.1 mW input optical power (b) and for the experimental optimal input optical power of 1.65 mW (d). Reported experimental powers are at the center laser wavelength and do not account for extra input power due to unfiltered ASE optical power coming from the EDFA. The data rate is 0.5 Gbps. Reported temperature and carrier averages and standard deviations are calculated over a 2 μs time series.

the power launched into the ring) and the difficulty of experimentally reaching the exact optimum operational point also contribute to this difference.

Due to the use of non-optimized grating couplers (with an insertion loss of around 10 dB) and a limited gain EDFA, the maximum input optical power that could be experimentally reached at the input waveguide of the modulator was around 2.6 mW. At high modulation speeds (a few Gbps) this amount of optical power would not result in significant nonlinear effects due to the slow thermal response of the device, which translates in lower thermal nonlinearities at the same level of input power. Therefore, in order to experimentally observe nonlinear phenomena at lower powers the data rate was reduced to 0.5 Gbps.

Figure 4 shows simulated and experimental transmission waveforms for low power (Fig. 4(a) - theoretical, Fig. 4(b) - experimental) and at the optimal input power (Fig. 4(c) - theoretical, Fig. 4(d) - experimental). The theoretical waveforms also show the thermal (red curve) and free carrier dispersion (green curve) temporal evolution (first and second terms in Eq. (1)). Again, good agreement between theoretical and experimental waveforms is obtained.

For low input powers (Figs. 4(a) and 4(b)) nonlinearities are weak, so resonance fluctuations are minimal and stable output power values for the '0' and '1' bits are achieved. At the optimal input power (Figs. 4(c) and 4(d)) the increase in temperature and carrier density variations generates visible fluctuations in the output power for bits '0' and '1'. Notice how our model correctly predicts the time evolution of the '0' and '1' levels observed experimentally: '1' output powers show a negative slope with time due to a temperature decrease (which moves the resonance towards shorter wavelengths and thus closer to the laser wavelength, as we concluded that optimal modulation is obtained with the laser on the blue side of the resonance), while '0' output powers show a positive slope with time due to the complementary effect (as we are closer to the resonance, there is a temperature increase which moves the resonance towards longer wavelengths and away from the operating laser wavelength). Notice how experimental '0' values do not reach close to zero transmission (as shown by simulation) due to the presence of noise.

As power is increased beyond the optimal point, the enhancement in thermal and carrier dispersion and corresponding '0' and '1' output power fluctuations is so high that the modulation performance decreases. To further explore the effects of high input powers over device performance, simulations were performed for input powers well above the optimum. The results are summarized in Fig. 5. As could be inferred from Fig. 3(c), the existence of an optimum input power beyond which modulation quality decreases is confirmed (Fig. 5(a)).

As power is increased beyond the maximum OMA point to 4.75 mW, an interesting trend is observed: the optimal operation results in bit 0 backing off from close to zero transmission (Fig. 5(b) for a 5 mW input power), showing that at such high powers it is necessary to keep the laser away from critical coupling in order to reduce the energy stored in the resonator and thus lower optical nonlinearities. This is also seen in Fig. 5(a), where the optimal wavelength moves toward shorter wavelengths for input powers above 4.75 mW (see the distinct knee in the red curve of Fig. 5(a)) . Figure 5(c) shows the resulting waveform at 5 mW input power if the laser is tuned closer to the resonance ($\lambda' = \lambda_{opt} + 800\ pm$) and critical coupling: thermal and free carrier dispersion effects are increased to a level that leads to very strong fluctuations in the '0' and '1' bits, and degradation of the modulation quality.

The agreement with experimental results at the modest data rates considered suggests that our theoretical model correctly captures the effects of both free carrier and thermal nonlinearities. Since modern data transmission devices work at speeds at least an order of magnitude higher than the 0.5 Gbps data rate considered in this work, it is pertinent to ask ourselves how does the behavior described here, and in particular the optimum input power, change as the data rate of the modulating signal is increased.

As bit time decreases well below the thermal time constant of the device ($\tau_{th} \approx 0.5\mu s$), the extent of thermal fluctuations (and thus its penalty on modulation efficiency) will decrease for the same input power due to the system's temperature not responding rapidly enough to the changes in the absorbed optical power. For the same reason, these thermal effects will become pattern dependent, that is, temperature changes will depend on how many consecutive '0' ('1') bits does the transmitting signal have, since this will set the maximum time the system has to increase (decrease) its temperature. Thus, for the same data pattern, an increase in the input optimal power with data rate is expected as it transitions from a bit time longer or comparable to the thermal time constant ($T_b > \approx \tau_{th}$) to a much shorter bit period ($T_b \ll \tau_{th}$). The increase in optimum power will stop when the decrease in bit time does not have a significant effect in the relative magnitude of T_b with respect to τ_{th}.

At data rates in which ($\tau_{th} \gg T_b > \tau_{fc}$), only free carrier effects will limit the maximum power that the device can handle. While the bit time is smaller than the free carrier lifetime, no change in the optimum power is expected, since the free carrier response won't be limited by the time the device stays on or off resonance. But if we keep increasing the data rate to a point in which T_b becomes comparable to τ_{fc}, the extent of carrier dispersion fluctuations (and thus its penalty on
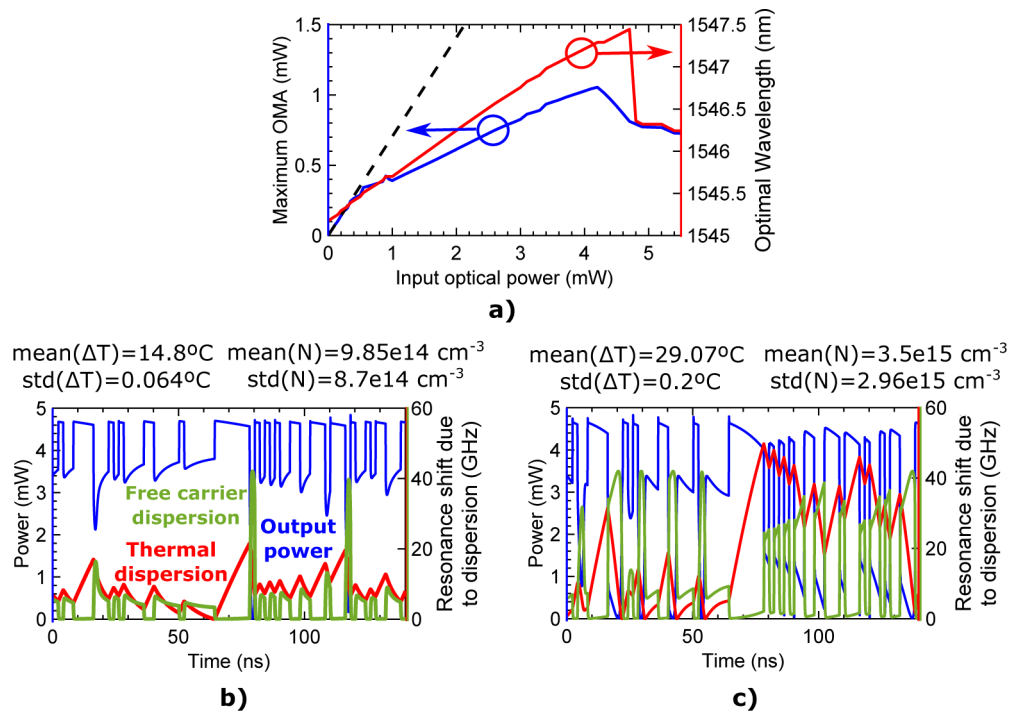
Fig. 5. Optimal operation point for high input optical powers. (a) Maximum attainable OMA (blue, left axis) and wavelength at which this value is reached (red, right axis) as a function of input power derived with the model. The dashed line shows the expected performance if no nonlinearities were present. (b)(c) Output optical power as a function of time (blue, left axis) and resonance frequency shift due to temperature (red, right axis) and carrier density (green, right axis) fluctuations for 5 mW of input optical power at the optimal operation wavelength of 1546.32 nm (b) and with a wavelength of 1547.52 nm, closer to the resonance (c). Resonance shifts are referenced to the minimum shift for the operational condition being considered, so that the shown curves are $\Delta W_X(t) - min\{\Delta W_X(t)\}$, where X refers to either temperature or carrier dispersion. Reported temperature and carrier averages and standard deviations are calculated over a 2 μs time series.

modulation efficiency) will decrease due to the free carrier population not being able to respond to changes in the bits being transmitted. At this point, both free carrier and thermal dispersion effects will become pattern dependent, and it is expected that for the same pattern there will be an increase in the optimum power as data rate increases.

The confirmation of this expected behavior through the time domain nonlinear model presented here is left for a follow-up paper.

5. Conclusion

We presented a time-domain model for silicon ring modulators under high input optical powers accounting for two-photon absorption, free-carrier absorption, thermal and dispersion effects to study the consequences of optical nonlinearities on modulation quality, and experimentally verified the theoretical results. We showed the existence of an optimal input optical power at which the best modulation performance (in terms of OMA) is achieved. Increasing the power beyond this point will degrade modulation by closing the eye diagram due to strong fluctuation in the resonance wavelength caused by thermal and free-carrier dispersion effects. The necessity

for correct initialization of the microring modulator through either tuning of the resonator or of the laser wavelength to place the device in the correct bi-stable state was also discussed.

These observations and the model derived here can be utilized for the design of practical microring modulators that will be needed for data-center optical interconnects or telecommunications systems.

Funding

Disclosures

R.J.R. is developing silicon photonic technologies at Ayar Labs, Inc.

References

1. D. A. B. Miller, "Rationale and challenges for optical interconnects to electronic chips," Proc. IEEE **88**(6), 728–749 (2000).
2. C. A. Brackett, "Dense wavelength division multiplexing networks: principles and applications," IEEE J. on Sel. Areas Commun. **8**(6), 948–964 (1990).
3. K. Preston, N. Sherwood-Droz, J. S. Levy, and M. Lipson, "Performance guidelines for WDM interconnects based on silicon microring resonators," in *CLEO: 2011 - Laser Science to Photonic Applications*, pp. 1–2 (2011).
4. A. Joshi, C. Batten, Y. J. Kwon, S. Beamer, I. Shamim, K. Asanovic, and V. Stojanovic, "Silicon-photonic clos networks for global on-chip communication," in *2009 3rd ACM/IEEE International Symposium on Networks-on-Chip*, pp. 124–133 (2009).
5. R. Soref and B. Bennett, "Electrooptical effects in silicon," IEEE J. Quantum Electron. **23**(1), 123–129 (1987).
6. Q. Xu, B. Schmidt, S. Pradhan, and M. Lipson, "Micrometre-scale silicon electro-optic modulator," Nature **435**(7040), 325–327 (2005).
7. E. Timurdogan, C. M. Sorace-Agaskar, J. Sun, E. S. Hosseini, A. Biberman, and M. R. Watts, "An ultralow power athermal silicon modulator," Nat. Commun. **5**(1), 4008 (2014).
8. M. Dinu, F. Quochi, and H. Garcia, "Third-order nonlinearities in silicon at telecom wavelengths," Appl. Phys. Lett. **82**(18), 2954–2956 (2003).
9. V. R. Almeida and M. Lipson, "Optical bistability on a silicon chip," Opt. Lett. **29**(20), 2387–2389 (2004).
10. Q. Xu and M. Lipson, "Carrier-induced optical bistability in silicon ring resonators," Opt. Lett. **31**(3), 341–343 (2006).
11. T. J. Johnson, M. Borselli, and O. Painter, "Self-induced optical modulation of the transmission through a high-Q silicon microdisk resonator," Opt. Express **14**(2), 817–831 (2006).
12. M. Soltani, S. Yegnanarayanan, Q. Li, A. A. Eftekhar, and A. Adibi, "Self-sustained gigahertz electronic oscillations in ultrahigh-*Q* photonic microresonators," Phys. Rev. A **85**(5), 053819 (2012).
13. S. M. Sze and K. K. Ng, *Physics of Semiconductor Devices* (John Wiley & Sons Ltd., 2006).
14. G. Treyz, "Silicon Mach-Zehnder waveguide interferometers operating at 1.3 μm," Electron. Lett. **27**(2), 118–120 (1991).
15. M. Borselli, T. J. Johnson, and O. Painter, "Accurate measurement of scattering and absorption loss in microphotonic devices," Opt. Lett. **32**(20), 2954–2956 (2007).
16. M. de Cea, A. H. Atabaki, L. Alloatti, M. Wade, M. Popovic, and R. J. Ram, "A thin silicon photonic platform for telecommunication wavelengths," in *2017 European Conference on Optical Communication (ECOC)*, pp. 1–3 (2017).
17. D. Dimitropoulos, R. Jhaveri, R. Claps, J. C. S. Woo, and B. Jalali, "Lifetime of photogenerated carriers in silicon-on-insulator rib waveguides," Appl. Phys. Lett. **86**(7), 071115 (2005).
18. G. Li, A. V. Krishnamoorthy, I. Shubin, J. Yao, Y. Luo, H. Thacker, X. Zheng, K. Raj, and J. E. Cunningham, "Ring resonator modulators in silicon for interchip photonic links," IEEE J. Sel. Top. Quantum Electron. **19**(6), 95–113 (2013).
19. J. T. Robinson, K. Preston, O. Painter, and M. Lipson, "First-principle derivation of gain in high-index-contrast waveguides," Opt. Express **16**(21), 16659–16669 (2008).
20. L. Shampine and M. Reichelt, "The MATLAB ODE suite," SIAM J. Sci. Comput. **18**(1), 1–22 (1997).
21. L. Alloatti, D. Cheian, and R. J. Ram, "High-speed modulator with interleaved junctions in zero-change CMOS photonics," Appl. Phys. Lett. **108**(13), 131101 (2016).
22. J. S. Orcutt, B. Moss, C. Sun, J. Leu, M. Georgas, J. Shainline, E. Zgraggen, H. Li, J. Sun, M. Weaver, S. Urošević, M. Popović, R. J. Ram, and V. Stojanović, "Open foundry platform for high-performance electronic-photonic integration," Opt. Express **20**(11), 12222–12232 (2012).

23. C. Sun, M. Wade, M. Georgas, S. Lin, L. Alloatti, B. Moss, R. Kumar, A. H. Atabaki, F. Pavanello, J. M. Shainline, J. S. Orcutt, R. J. Ram, M. Popović, and V. Stojanović, "A 45 nm CMOS-SOI monolithic photonics platform with bit-statistics-based resonant microring thermal tuning," IEEE J. Solid-State Circuits **51**(4), 893–907 (2016).
24. G. P. Agrawal, *Fiber-Optic Communication Systems* (John Wiley & Sons, Inc., 2011).
25. T. Carmon, T. J. Kippenberg, L. Yang, H. Rokhsari, S. Spillane, and K. J. Vahala, "Feedback control of ultra-high-Q microcavities: application to micro-raman lasers and micro-parametric oscillators," Opt. Express **13**(9), 3558–3566 (2005).